ELSEVIER

Ocean Modelling 5 (2002) 17–35

Ocean Modelling

www.elsevier.com/locate/omodol

A comparison of three finite elements to solve the linear shallow water equations

E. Hanert [a,b,*], V. Legat [a], E. Deleersnijder [b]

[a] *Centre for Systems Engineering and Applied Mechanics, Université Catholique de Louvain, 4 Avenue Georges Lemaître, B-1348 Louvain-la-Neuve, Belgium*

[b] *Institut d'Astronomie et de Géophysique G. Lemaître, Université Catholique de Louvain, 2 Chemin du Cyclotron, B-1348 Louvain-la-Neuve, Belgium*

Received 11 January 2002; received in revised form 26 March 2002; accepted 26 March 2002

Abstract

The purpose of the present study is to select a convenient mixed finite element formulation for ocean modelling. The finite element equivalents of Arakawa's A-, B- and C-grids are investigated by using the linear shallow water equations. Numerical and analytical techniques are used to study the types of computational noise present in each element. It is shown that the P_1P_1 and the P_1P_0 element (the equivalents of the A- and B-grids respectively) allow the presence of spurious computational modes in the elevation field. For the P_1P_1 element, these modes can be filtered out by adding a stabilizing term to the continuity equation. This method, although consistent, can lead to dissipative unphysical effects at the discrete level. The $P_1^{\perp}P_0$ element or low order Raviart–Thomas element (corresponding to the C-grid) is free of elevation noise and represents well inertia-gravity waves when the deformation radius is resolved but presents computational velocity modes. These modes are however filtered out in a more complex model in which the momentum diffusion term is not neglected.

Keywords: Ocean modelling; Unstructured grids; Finite elements; Spurious computational modes

1. Introduction

The first ocean general circulation model (OGCM) was created by Bryan at the end of 1960's (Bryan, 1969). The spatial discretization of this model was based on a structured grid and a finite

* Corresponding author. Address: Institut d'Astronomie et de Géophysique G. Lemaître, Université Catholique de Louvain, 2 Chemin du Cyclotron, B-1348 Louvain-la-Neuve, Belgium.

E-mail address: hanert@astr.ucl.ac.be (E. Hanert).

1463-5003/02/$ - see front matter
PII: S1463-5003(02)00012-4

difference scheme. Since then, there has been a lot of improvements to the initial model of Bryan but the large majority of today OGCMs are still based on a finite difference scheme. This is mainly due to the inherent simplicity of structured grids (Haidvogel and Beckmann, 1999). More recently, general and coastal circulation models using a more advanced and less traditional approach have been built (e.g. Le Provost et al., 1994; Myers and Weaver, 1995; Lynch et al., 1996). These numerical models are based on the finite element method. Such a method, mainly used in engineering, could be an interesting alternative to the finite difference method.

The chief advantage of the finite element method over the finite difference method is its faculty to deal with unstructured grids. This kind of grid is attractive for different reasons. First of all, it permits to represent much more easily irregular domains. This is very useful in oceanography where uneven coastlines, narrow straits and islands are numerous. The use of an unstructured grid also allows to achieve high resolution in regions of interest thanks to convenient grid refinements. Thus, the computational effort is concentrated where the flow necessitates it and not elsewhere. The representation of western boundary currents is greatly improved since high resolution is only required in the boundary layer and not in the less active interior ocean. Finally, structured grids based on the geographical coordinates are plagued with difficulties near the North Pole (Murray and Reason, 2002). This is due to the convergence of the meridians which requires unacceptably small time steps to maintain stability. This constraint is irrelevant in a model using an unstructured grid.

Furthermore, the finite element method rests on a rigorous mathematical framework based on a weighted residuals formulation which permits a precise definition of notions such as the error, convergence rate and stability conditions. Neumann boundary conditions are easily applied as they enter the weak statement of the problem directly with no further impositions or approximations (Myers and Weaver, 1995).

A critical issue to apply the finite element method in oceanography is to find a suitable finite element pair for velocity and surface elevation (pressure). This pair should represent geophysical flows correctly and not allow the existence of spurious computational modes. It should also be mass preserving as the numerical model is aimed to be used for long term simulations. For the moment, there is no element which entirely fulfills these requirements and hence it is still necessary to compare finite element discretizations in the context of ocean modelling.

Therefore, in the present study, we compare the finite element equivalents of the A-, B- and C-grids of Mesinger and Arakawa (1976) and analyze their numerical behaviour while representing a geophysical flow. Since the A-, B- and C-grids are widely used in ocean modelling and have acknowledged qualities, it seems interesting to see if their finite element equivalents have similar properties.

To compare these three finite element discretizations, we have solved the linear, inviscid shallow water equations (SWE). Thanks to their inherent simplicity, these equations are the traditional test case problem to select an appropriate spatial discretization. They have been widely used for assessing finite difference and finite element discretizations (e.g. Batteen and Han, 1981; Walters and Carey, 1984; Le Roux et al., 1998). The shallow water model is also the simplest geophysical model allowing the existence of inertia-gravity waves. Since the propagation of these waves is now taken into account in modern numerical models, it is of paramount importance that the numerical scheme used to simulate them behaves properly.

The paper is organized as follows. In the next section, we specify the model equations and their finite elements discretization. In Section 3, we examine the three finite elements considered and see if they support spurious numerical oscillations. Stabilization techniques and conservation issues are discussed in Sections 4 and 5 respectively. Finally, numerical simulations results are given in Section 6.

2. Finite element discretization of the linear SWE

2.1. Continuous problem

The SWE describe incompressible, free surface flows in which the vertical pressure is hydrostatic. These equations are derived from the Navier–Stokes equations by integration over the depth of the fluid layer. The two-dimensional, inviscid, linear form of the SWE reads

$$\frac{\partial \eta}{\partial t} + H\left(\frac{\partial u}{\partial x} + \frac{\partial v}{\partial y}\right) = 0, \tag{1}$$

$$\frac{\partial u}{\partial t} - fv + g\frac{\partial \eta}{\partial x} = 0, \tag{2}$$

$$\frac{\partial u}{\partial t} + fu + g\frac{\partial \eta}{\partial y} = 0, \tag{3}$$

where η is the surface elevation measured from a reference height, H is the unperturbed depth of the water column which is taken to be constant here, u and v are the depth-averaged velocity components in the x- and y-directions respectively, g is the gravitational acceleration and t is time. A more complete derivation of these equations may be found in LeBlond and Mysak (1978).

2.2. Finite element approximation

Let Ω be the model domain with boundary Γ and let $\mathbf{n}$ be the outward unit normal vector. Let $\mathbf{u} = (u, v)$ be in a suitable functional space V such that $\mathbf{u} \cdot \mathbf{n} = 0$ on Γ for all $\mathbf{u}$ belonging to V. Finally let η be in W, the space of square integrable functions on Ω.

The weak formulation of Eqs. (1)–(3) in their vector form is found by integrating these equations against a set of admissible test functions $\boldsymbol{\varphi}$ and ψ belonging to the same function space as $\mathbf{u}$ and η. Thus ($\mathbf{u}$, η) satisfy

$$\frac{\mathrm{d}}{\mathrm{d}t}\int_\Omega \eta\psi \,\mathrm{d}\Omega + H\int_\Omega \nabla\cdot\mathbf{u}\psi \,\mathrm{d}\Omega = 0, \tag{4}$$

$$\frac{\mathrm{d}}{\mathrm{d}t}\int_\Omega \mathbf{u}\cdot\boldsymbol{\varphi} \,\mathrm{d}\Omega + f\int_\Omega (\mathbf{e}_z \times \mathbf{u})\cdot\boldsymbol{\varphi} \,\mathrm{d}\Omega + g\int_\Omega \nabla\eta\cdot\boldsymbol{\varphi} \,\mathrm{d}\Omega = 0. \tag{5}$$

Eq. (5) is integrated by parts to remove elevation derivatives and thus to avoid having to impose boundary conditions on the elevation field:

$$\int_\Omega \nabla\eta\cdot\boldsymbol{\varphi} \,\mathrm{d}\Omega = -\int_\Omega \eta\nabla\cdot\boldsymbol{\varphi} \,\mathrm{d}\Omega + \int_\Gamma \eta\boldsymbol{\varphi}\cdot\mathbf{n} \,\mathrm{d}\Gamma. \tag{6}$$

The second term on the right hand side of (6) vanishes since $\boldsymbol{\varphi} \in V$ and so $\boldsymbol{\varphi} \cdot \mathbf{n} = 0$.

In the Galerkin procedure, an approximate solution $(\mathbf{u}^h, \eta^h)$ in the finite dimensional subspace (V^h, W^h) of the infinite dimensional space (V, W) is sought. The approximate solutions $\mathbf{u}^h$ and η^h are typically piecewise-polynomials (not necessarily of the same degree) satisfying the essential boundary conditions and such that (4) and (5) hold for any admissible test functions $\boldsymbol{\varphi}^h \in V^h$ and $\psi^h \in W^h$.

Let us now define a finite element triangulation of the model domain Ω and let $\varphi_j \equiv \varphi_j(\mathbf{x})$, $j = 1, \ldots, N$ and $\psi_j, j = 1, \ldots, M$ be piecewise-polynomial finite element basis functions spanning the approximation spaces V^h and W^h respectively. Then, for any pair $(\mathbf{u}^h, \eta^h)$ in $V^h \times W^h$ we have the expressions

$$\mathbf{u}^h(\mathbf{x}) = \sum_{j=1}^{N} \mathbf{u}_j \varphi_j(\mathbf{x}), \tag{7}$$

$$\eta^h(\mathbf{x}) = \sum_{j=1}^{M} \eta_j \psi_j(\mathbf{x}), \tag{8}$$

where N and M are the number of velocity and elevation nodes respectively. By applying the Galerkin procedure (which orthogonalizes the residual error to the basis functions for the L^2 square product), Eqs. (4) and (5) can be summarized as seeking the nodal values $\mathbf{u}_j$ and η_j such that

$$\sum_{j=1}^{M} \frac{\mathrm{d}\eta_j}{\mathrm{d}t} \int_\Omega \psi_m \psi_j \,\mathrm{d}\Omega + H \sum_{j=1}^{N} \mathbf{u}_j \cdot \int_\Omega \psi_m \nabla \varphi_j \,\mathrm{d}\Omega = 0 \quad \text{for } m = 1, \ldots, M, \tag{9}$$

$$\sum_{j=1}^{N} \frac{\mathrm{d}\mathbf{u}_j}{\mathrm{d}t} \int_\Omega \varphi_m \varphi_j \,\mathrm{d}\Omega + f \sum_{j=1}^{N} (\mathbf{e}_z \times \mathbf{u}_j) \int_\Omega \varphi_m \varphi_j \,\mathrm{d}\Omega - \sum_{j=1}^{M} g\eta_j \int_\Omega \nabla \varphi_m \psi_j \,\mathrm{d}\Omega = 0 \quad \text{for } m = 1, \ldots, N. \tag{10}$$

By evaluating the integrals in Eqs. (9) and (10) and discretizing the temporal derivatives, a linear system for the nodal values $\mathbf{u}_j$ and η_j can be found.

3. Mixed finite element formulation

In this section, the triangular finite elements corresponding to Arakawa's A-, B- and C-grids are compared (Fig. 1). It is shown that these three elements allow the existence of either spurious elevation or velocity modes.

Spurious modes are internode oscillations either in the elevation or in the velocity field. More precisely, spurious elevation modes are non-constant eigenvectors of the discrete gradient operator with zero eigenvalues. If Q is the discrete gradient operator then η^h is a spurious elevation mode if $Q\eta^h = 0$ with η^h non-constant. Spurious velocity modes can also be found. These modes are non-zero eigenvectors of the discrete Coriolis operator with zero eigenvalue. Thus if F is the discrete Coriolis operator then $\mathbf{u}^h$ is a spurious velocity mode if $F\mathbf{u}^h = 0$ with $\mathbf{u}^h$ non-zero. All

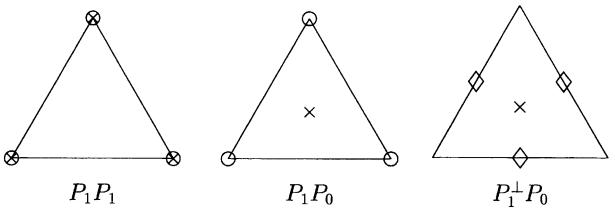

Fig. 1. The triangular finite elements compared in this section. The symbols "$\circ$", "$\times$" and "$\diamondsuit$" indicate full velocity nodes, surface-elevation nodes and normal velocity nodes respectively.

these spurious modes are not seen by the scheme and can be added to any solution of the problem considered. As a result, they will have to be filtered out in order to use the corresponding element to solve the SWE.

3.1. P_1P_1 element

This element is piecewise linear for elevation and velocity (Fig. 1). Let us consider the null-space of the discretized gradient operator Q, defined as follows:

$$Q\eta^h = \int_{\Omega_0} \eta^h \nabla \varphi_i \, \mathrm{d}\Omega, \tag{11}$$

where Ω_0 is the support of a velocity basis function φ_i corresponding to an internal velocity node denoted by i (Fig. 2). The expansion of η in terms of linear shape functions in (11) gives the 2×6 linear system:

$$2(\eta_2 - \eta_5) + \eta_3 - \eta_4 + \eta_1 - \eta_6 = 0, \tag{12}$$

$$2(\eta_4 - \eta_1) + \eta_3 - \eta_2 + \eta_5 - \eta_6 = 0. \tag{13}$$

The general solution of (12) and (13) is of the form $(\eta_1, \eta_2, \eta_3, \eta_4, \eta_5, \eta_6) = (a, b, c, a+ d, b - d, c + d)$ where a, b, c, d are arbitrary constants (Le Roux et al., 1998). There are four degrees of freedom corresponding to four possible solutions. One of these is the constant elevation field and the three others are spurious modes. Thus, if nothing is done to suppress spurious pressure modes, the P_1P_1 element does not seem to be a good candidate to solve the SWE.

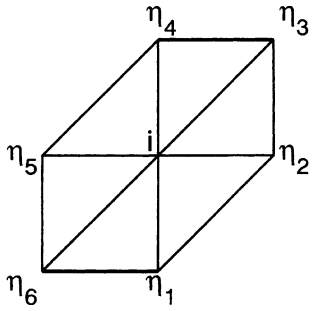

Fig. 2. Velocity node i and the surrounding elevation nodes for the P_1P_1 element.

3.2. P_1P_0 element

This element is piecewise linear for velocity and piecewise constant for elevation (Fig. 1). Let us consider the velocity shape function support in Fig. 3 and see if it permits the existence of spurious elevation modes. The expansion of η in terms of constant polynomials in (11) gives the following 2×6 linear system:

$$(\eta_1 + \eta_6) - (\eta_3 + \eta_4) = 0, \tag{14}$$

$$(\eta_2 + \eta_3) - (\eta_5 + \eta_6) = 0. \tag{15}$$

These equations still permit the existence of a checkerboard surface elevation, e.g. $(\eta_1, \eta_2, \eta_3, \eta_4, \eta_5, \eta_6) = (a, -a, a, -a, -a, a)$. Again, it seems that this element is not a good candidate to solve the SWE.

3.3. $P_1^{\perp}P_0$ element

The $P_1^{\perp}$ symbol denotes an element with normal velocity nodes in the middle of each edge of the triangulation and the P_0 symbol has the same signification as before (Fig. 1). This element, also called low order Raviart–Thomas element (Raviart and Thomas, 1977), is based on flux conservation on elements edges and the resulting scheme is very close to a finite volume scheme. A shallow water model using this element is described in Miglio et al. (1999).

The velocity is approximated in the following way:

$$\mathbf{u} \simeq \mathbf{u}^h = \sum_{i=0}^{N_{\mathrm{ed}}} J_i \boldsymbol{\varphi}_i, \tag{16}$$

with J_i, the normal flux through the edge Γ_i, as a generalized scalar nodal value and N_{ed}, the number of edges of the triangulation. On a given element Ω_e of the triangulation, the restriction of the vector shape function is given by

$$\boldsymbol{\varphi}_i(\mathbf{x})|_{\Omega_e} = \frac{\mathbf{x} - \mathbf{x}_i}{2|\Omega_e|}, \tag{17}$$

where $|\Omega_e|$ is the surface of the element and $\mathbf{x}_i$ is the coordinate of the vertex i opposite to the edge Γ_i, (Fig. 4). For this element, we have the following properties:

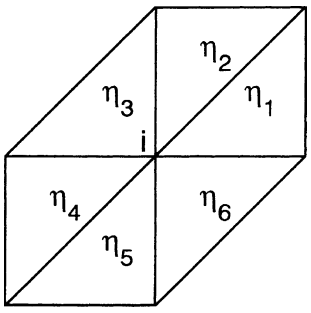

Fig. 3. Velocity node i and the surrounding elevation nodes for the P_1P_0 element.

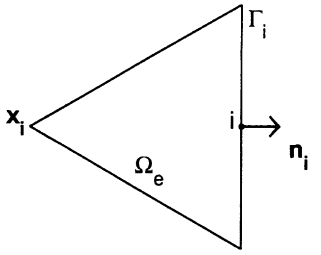

Fig. 4. Some notations for the $P_1^{\perp}P_0$ element.

$$\nabla \cdot \boldsymbol{\varphi}_i|_{\Omega_e} = \frac{1}{|\Omega_e|},$$

$$\boldsymbol{\varphi}_i|_{\Omega_e} \cdot \mathbf{n}_m = \frac{\delta_{im}}{|\Gamma_m|},$$

where $\mathbf{n}_m$ is the outward normal to the edge Γ_m and $|\Gamma_m|$ is the length of Γ_m.

To see if this element allows the existence of spurious elevation modes, we consider a velocity node i and its support (Fig. 5). By computing expression (11) for this support with the previously defined shape functions, we obtain the following expression:

$$\eta_1 - \eta_2 = 0. \tag{18}$$

The solution of this equation can only be a constant elevation field and thus the $P_1^{\perp}P_0$ element does not present any spurious elevation modes. However, this element allows the existence of spurious velocity modes. This can be seen by considering the discrete Coriolis operator (F) defined as follows:

$$F\mathbf{u}^h \equiv \int_{\Omega} (\mathbf{e}_z \times \mathbf{u}^h) \cdot \boldsymbol{\varphi}_i \, \mathrm{d}\Omega \tag{19}$$

and its null space. By considering a velocity node i and its support (Fig. 5) and imposing that $F\mathbf{u}^h = 0$, the following relation is obtained:

$$(J_1 - J_2) + (J_4 - J_3) = 0, \tag{20}$$

which admits non-zero solutions. These non-trivial solutions are also called spurious "f-modes".

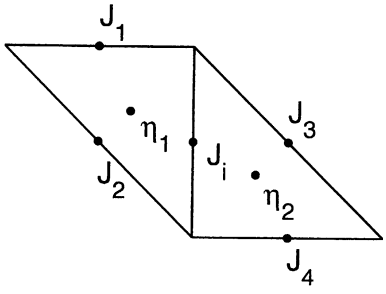

Fig. 5. Velocity node i and the surrounding elevation and velocity nodes for the $P_1^{\perp}P_0$ element.

Spurious velocity modes also arise in finite differences with Arakawa C-grid because of the averaging in the discrete Coriolis operator (Batteen and Han, 1981). Methods have been suggested to avoid them (e.g. Adcroft et al., 1999) and to still be able to use the C-grid in large scale ocean models. Further researches are needed to "transfer" these techniques to finite elements. However, these spurious modes can be filtered out easily if a diffusion term is added to the velocity equation.

Once the normal fluxes are computed, it is possible to find the normal velocity at each side of the triangulation and then to compute the full velocity at the vertices of each triangle. The full velocity at mid-sides is found by interpolating the velocity field between vertices (Walters and Casulli, 1998).

The presence of normal velocity nodes at mid-sides permits to apply easily no-normal flow boundary conditions. A drawback of P_1P_1 and P_1P_0 elements is that the normal vector at boundary nodes has to be computed to apply no-normal flow boundary conditions. The way to define this normal vector is not univocal; one way to define it is given by Engelman et al. (1982).

4. Stabilization techniques

All the three elements introduced before allow the existence of spurious computational modes (either for elevation or velocity). If we want to use one of these elements to solve the SWE or a more complex ocean circulation model, spurious modes should be filtered out. Noise control procedures, also called stabilization techniques, are presented in this section.

4.1. Spurious elevation modes

These modes are high frequency oscillations which can be added to any correct elevation field. The easiest way to stabilize the elevation is to add a Laplacian term to the continuity equation and thus to consider the following equation:

$$\frac{\partial \eta}{\partial t} + H\left(\frac{\partial u}{\partial x} + \frac{\partial v}{\partial y}\right) = \alpha \nabla^2 \eta \tag{21}$$

instead of Eq. (1). The parameter α is an appropriate diffusivity which can be tuned to an optimal value such that the computational modes are filtered out with α as small as possible. The discretization of Eq. (21) yields a coupling of neighboring elevation unknowns, and consequently has a smoothing effect (DeMulder, 1997). However, this approach violates consistency, since the exact solution of the SWE does not satisfy (21).

A consistent stabilization term can be found by taking the divergence of Eqs. (2) and (3). This term reads:

$$\nabla^2 \eta + \frac{1}{g}\frac{\partial}{\partial t}(\nabla \cdot \mathbf{u}) + \frac{f}{g}\nabla \cdot (\mathbf{e}_z \times \mathbf{u}). \tag{22}$$

By multiplying this term by a elevation shape function (ψ), integrating it by parts on the whole computational domain and applying it to the approximate solution ($\mathbf{u}^h$, η^h), the following stabilization term is obtained for the discrete formulation:

$$-\int_\Omega \nabla \eta^h \cdot \nabla \psi \, \mathrm{d}\Omega + \frac{1}{g}\int_\Omega \frac{\partial}{\partial t}(\nabla \cdot \mathbf{u}^h)\psi \, \mathrm{d}\Omega - \frac{f}{g}\int_\Omega (\mathbf{e}_z \times \mathbf{u}^h) \cdot \nabla \psi \, \mathrm{d}\Omega, \tag{23}$$

where the following natural boundary conditions have been used for the tangential velocity and the elevation:

$$\frac{f}{g}\int_{\Gamma}\psi(\mathbf{e}_z\times\mathbf{u}^h)\cdot\mathbf{n}\,\mathrm{d}\Gamma+\int_{\Gamma}\psi\nabla\eta^h\cdot\mathbf{n}\,\mathrm{d}\Gamma=0. \tag{24}$$

The problem can then be stabilized by adding (23) multiplied by an appropriate diffusivity (α) to the continuity equation in its weak formulation. This method is used in Section 6 to stabilize the P_1P_1 element.

It must be pointed out that the two stabilization methods presented in this section only work if the elevation field is approximated by shape functions of degree one or more. As a result, only the P_1P_1 element can be stabilized by using these methods. Moreover, these methods lead to the addition of a diffusion term to the continuity equation. This manipulation is numerically efficient but has no physical justification since there are no mass diffusion processes. However, a diffusion term is frequently added to the continuity equation in finite difference ocean models to stabilize the B-grid (e.g. Killworth et al., 1991 or Deleersnijder and Campin, 1995).

4.2. Spurious velocity modes

To control the computational modes generated by the discretization of the Coriolis force with the $P_1^{\perp}P_0$ element, a diffusion term should be added to the momentum equation. This yields a coupling between neighboring velocity unknowns and filters out high frequency oscillations. Thus, the following momentum equation should be considered

$$\frac{\partial\mathbf{u}}{\partial t}+f\mathbf{e}_z\times\mathbf{u}=-g\nabla\eta+\nu\nabla^2\mathbf{u}, \tag{25}$$

where ν is the viscosity of the flow.

Of course, the exact solution of the SWE equations does not satisfy Eq. (25) but the Laplacian term in this equation is physically realistic since there are momentum diffusion processes. In a more complex and more realistic ocean model, the momentum diffusion term is not neglected and thus spurious velocity modes generated by the $P_1^{\perp}P_0$ element would be filtered out (Hanert et al., submitted for publication). Numerical experiments have been performed in order to see the viscosity minimal value which suppresses the computational modes.

5. Temporal discretization and conservation issues

The time discretization of Eqs. (1)–(3) is based on a semi-implicit Crank–Nicolson scheme. It is shown hereafter that this temporal discretization has interesting conservative properties. The semi-discrete equations read:

$$\mathbf{u}^{n+1}+\frac{f\Delta t}{2}\mathbf{e}_z\times\mathbf{u}^{n+1}+\frac{g\Delta t}{2}\nabla\eta^{n+1}=\mathbf{u}^n-\frac{f\Delta t}{2}\mathbf{e}_z\times\mathbf{u}^n-\frac{g\Delta t}{2}\nabla\eta^n, \tag{26}$$

$$\eta^{\eta+1}+\frac{H\Delta t}{2}\nabla\cdot\mathbf{u}^{n+1}=\eta^n-\frac{H\Delta t}{2}\nabla\cdot\mathbf{u}^n, \tag{27}$$

where $\mathbf{u}^n$ denotes the velocity field at the previous time step and $\mathbf{u}^{n+1}$, the velocity field at the current time step.

A key quantity to be conserved by the numerical model is the total amount of water. This is especially important for long term simulations where even a negligible water gain or loss at each time step could have disastrous consequences. The fluid being incompressible, conservation can be checked by integrating the elevation field on the whole domain and verifying that this quantity is constant in time. The total amount of fluid is obviously conserved for the exact problem. For the discrete problem, the continuity equation in its weak formulation in terms of $\mathbf{u}^h$ and η^h has to be considered:

$$\int_\Omega \frac{\partial \eta^h}{\partial t}\psi_j \,\mathrm{d}\Omega + H\int_\Omega \nabla\cdot\mathbf{u}^h\psi_j \,\mathrm{d}\Omega = 0. \tag{28}$$

By using the fact that the sum of all the shape functions is equal to one, we obtain:

$$\int_\Omega \frac{\partial \eta^h}{\partial t}\,\mathrm{d}\Omega = -H\int_\Omega \nabla\cdot\mathbf{u}^h\,\mathrm{d}\Omega = -H\int_\Gamma \mathbf{u}^h\cdot\mathbf{n}\,\mathrm{d}\Gamma = 0. \tag{29}$$

Mass conservation is thus ensured by imposing no-normal flow boundary conditions and computing the integrals exactly. This last condition requires to increase the numerical integration order as the shape functions order is increased.

Let us now show that the total energy of the flow is conserved if a semi-implicit time discretization is used. The total energy of the flow is defined as follows:

$$E = \frac{1}{2}\int_\Omega \rho(H\mathbf{u}^2 + g\eta^2)\,\mathrm{d}\Omega, \tag{30}$$

where ρ is the density of the fluid, supposed to be constant. The energy time derivative reads:

$$\frac{\mathrm{d}E}{\mathrm{d}t} = \int_\Omega \rho\left(H\mathbf{u}\cdot\frac{\partial\mathbf{u}}{\partial t} + g\eta\frac{\partial\eta}{\partial t}\right)\mathrm{d}\Omega. \tag{31}$$

By discretizing all the terms in the previous equation semi-implicitly and using Eqs. (26) and (27), the following semi-discrete relation is obtained:

$$\begin{aligned}\frac{E^{n+1}-E^n}{\Delta t} = \int_\Omega \rho H\frac{\mathbf{u}^{n+1}+\mathbf{u}^n}{2}\cdot\left[-f\mathbf{e}_z\times\frac{\mathbf{u}^{n+1}+\mathbf{u}^n}{2} - g\nabla\left(\frac{\eta^{n+1}+\eta^n}{2}\right)\right]\\ + \rho g\frac{\eta^{n+1}+\eta^n}{2}\left[-H\nabla\cdot\left(\frac{\mathbf{u}^{n+1}+\mathbf{u}^n}{2}\right)\right]\mathrm{d}\Omega.\end{aligned} \tag{32}$$

After some algebraic manipulations, we finally obtain:

$$\frac{E^{n+1}-E^n}{\Delta t} = \rho g H\int_\Gamma \frac{\eta^{n+1}+\eta^n}{2}\,\frac{\mathbf{u}^{n+1}+\mathbf{u}^n}{2}\cdot\mathbf{n}\,\mathrm{d}\Omega = 0. \tag{33}$$

The use of a semi-implicit time discretization has thus several advantages, it preserves the total energy of the flow and permits to circumvent the strong Courant–Friedrichs–Lewy (CFL) constraint on the time step. It should however be pointed out that the time step is still limited by accuracy requirements in practice. It can easily be seen that energy conservation holds for the discrete problem by considering the discrete equations and recalling that $\mathbf{u}^h$ and η^h are linear combinations of shape functions. Hence, a semi-implicit finite element discretization of the in-

viscid SWE is totally energy preserving. Since it holds for the totally discrete equations, this result goes a step further than results found by Lilly (1965) for the semi-discrete equations.

It should be pointed out that the use of a semi-implicit scheme requires to solve a linear system at each time step. To solve such a system, it is possible to use direct or iterative solvers. The use of a direct solver guarantees that a solution will be produced for a well-posed problem but the memory storage required and the CPU needed might be very large, especially for a global circulation problem where those requirements can become prohibitive. Iterative methods would then become attractive. However, it is beyond the scope of this work to analyze the performance of iterative methods. Our main concern is the analysis of mixed finite element formulations for the SWE. Hence, we use a standard direct frontal method to solve the discrete system (Iron, 1970; Leygue and Legat, 2000).

6. Numerical simulations

In this section, numerical experiments are performed in order to compare the different triangular finite elements introduced previously. These experiments have allowed us to show that the P_1P_1 and P_1P_0 elements can generate spurious elevation modes unlike the $P_1^{\perp}P_0$ element. It is shown that these spurious elevation oscillation are filtered out when the P_1P_1 element is stabilized by adding a diffusion term to the continuity equation. Some experiments have also been performed to see if the addition of a diffusion term to the momentum equation prevents the occurrence of spurious velocity modes for the $P_1^{\perp}P_0$ element. Eventually it is shown that the $P_1^{\perp}P_0$ and the stabilized P_1P_1 element are both mass preserving but that the stabilization technique used for the P_1P_1 scheme leads to a decrease in the total energy of the flow.

6.1. High frequency elevation modes

In this section the same numerical experiment as in Batteen and Han (1981) is performed in order to compare the three triangular finite elements described before. In their paper, Batteen and Han showed the condition of appearance of spurious elevation modes in finite differences for Arakawa B- and C-grids by strongly forcing the short wave modes.

They used a rectangular basin with zero normal velocity at boundaries and the fluid initially at rest. A point mass source and sink were used to force the flow. Solutions for the height field after a hundred time steps were presented according to the ratio of the Rossby radius of deformation ($R \equiv \sqrt{gh}/f$) to the grid size (d). The finite difference B-scheme displayed a checkerboard pattern of noise in both the gravity wave ($R/d > 1$) and inertial ($R/d < 1$) limit. The C-scheme displayed an oscillatory noise only for the inertial limit.

In the present experiment, we solve the inviscid SWE ($\nu = 0$) and only consider the effect of a mass diffusion term. We use a square basin of 1000 km side covered with a structured mesh of rectangular triangles (Fig. 6). The longest edge of each triangle is equal to 62.5 km and the grid size is supposed to be equal to 50 km. Numerical simulations are performed in both the inertial ($R/d = 1/4$) and the gravity wave ($R/d = 2$) limit. A point mass source and a point mass sink of 1 and -1 m respectively are prescribed at fixed locations, on an horizontal line in the middle of the domain, 500 km apart at each time step. The Coriolis parameter and the gravitational acceleration

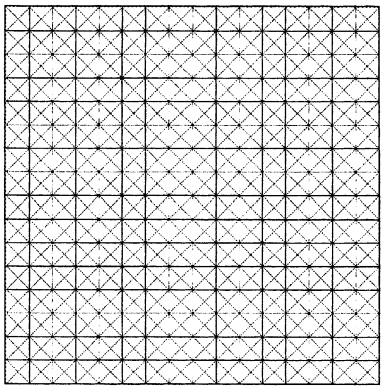

Fig. 6. Structured mesh used for high frequency modes simulation. This mesh has 1024 elements.

are set to 10^{-4} s^{-1} and 10 m s^{-2} respectively. The mean depth of the water column is set to 10 and 10/64 m in order to have $R/d = 2$ and 1/4 respectively. The time step is set to 100 s for $R/d = 2$ and 800 s for $R/d = 1/4$ in order to have the same CFL number in both limits.

Regardless of the (R/d) ratio, the P_1P_1 element presents a noisy elevation pattern. This is due to the averaging in the pressure gradient force, which allows the existence of spurious elevation modes (Fig. 7). These spurious modes are removed when the stabilization term (22) is added to the continuity equation with a diffusivity coefficient, α, set to 5×10^5 m^2/s. Fig. 8 shows that the noise in the elevation field has been totally suppressed.

The P_1P_0 element presents the same drawbacks as the P_1P_1 element. For both high and low resolutions, the elevation field is polluted by spurious oscillations (Fig. 9). This element can however not be stabilized by adding a diffusion term to the continuity equation since its elevation shape functions are constant.

In the previous section, it was seen that the $P_1^{\perp}P_0$ element is the only element which does not present spurious elevation modes (only spurious velocity modes) and thus, in the gravity wave

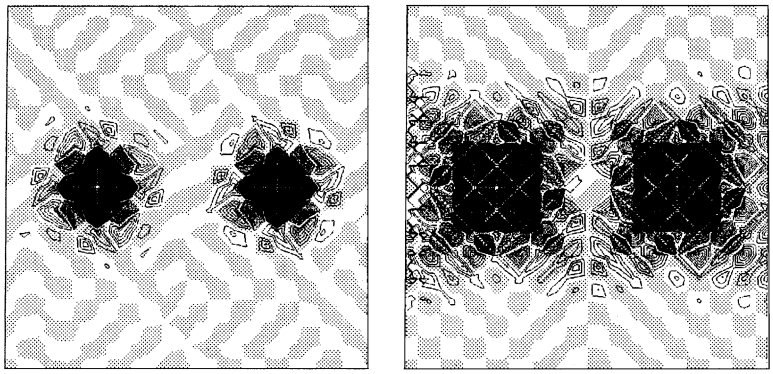

Fig. 7. Isolines of the surface-elevation field for the P_1P_1 element for $R/d = 1/4$ (left) and $R/d = 2$ (right). In all elevation fields which follow, white and grey regions denote positive and negative elevation values respectively. The contour interval is 0.1 m. For both schemes the locations of the source and sink regions are to the left and the right, respectively, of the center point in each figure.

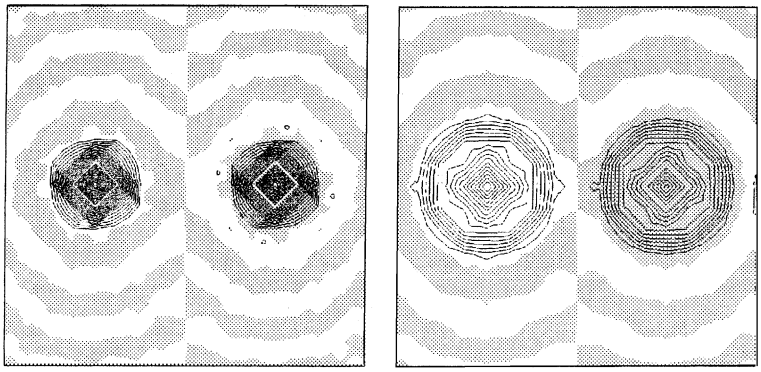

Fig. 8. Same as Fig. 7 for the stabilized P_1P_1 element ($\alpha = 5 \times 10^5$ m^2/s).

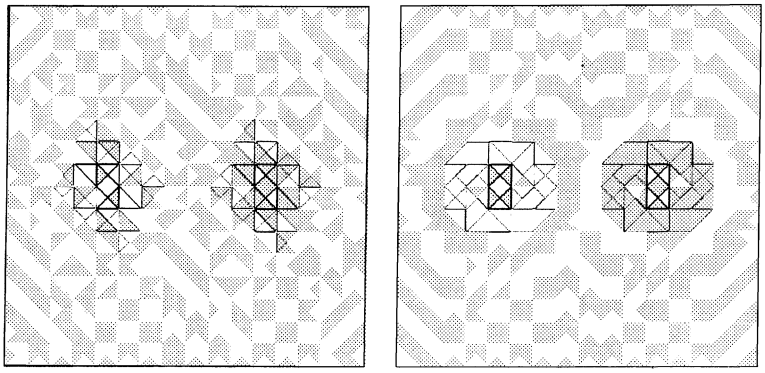

Fig. 9. Same as Fig. 7 for the P_1P_0 element.

limit, the elevation field should be well represented. This is actually the case and the geostrophic adjustment is well represented. However, when the Coriolis term dominates the pressure gradient term (inertial limit), problems appear as the $P_1^{\perp}P_0$ element propagates badly inertia-gravity waves when the Rossby deformation radius is not resolved (Fig. 10). These problems are the same as those encountered by the finite difference C-grid.

These results are similar to those found by Batteen and Han (1981) for the corresponding finite difference discretizations. When the deformation radius is not resolved, all the elements represent badly geostrophic adjustment processes. When, the deformation radius is resolved, the $P_1^{\perp}P_0$ is the only "non-stabilized" element to represent correctly the geostrophic adjustment without any noise in the elevation field. The P_1P_1 and P_1P_0 elements are plagued with spurious elevation modes. Those modes are suppressed when the P_1P_1 element is stabilized.

6.2. High frequency velocity modes

Let us now show that the resolution of the SWE with the $P_1^{\perp}P_0$ element can generate spurious velocity modes if the momentum diffusion term is neglected. If this term is not neglected, it is

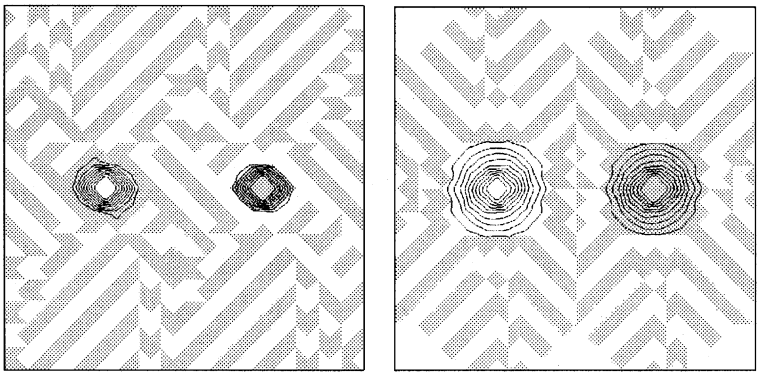

Fig. 10. Same as Fig. 7 for the $P_1^{\perp}P_0$ element.

possible to find a threshold viscosity value to filter out the velocity modes. In this section, we only consider the effect of the momentum diffusion term ($\nu \neq 0$) and there is no diffusion term in the continuity equation ($\alpha = 0$).

For this experiment, a square basin of 1000 km side is used with the same structured mesh as before. The depth of the water column, the Coriolis parameter, the gravitational acceleration and the time step are set to 2000 m, 10^{-4} s^{-1}, 10 m s^{-2} and 100 s respectively. As initial conditions, the elevation and the velocity are set to zero except at one point in the middle of the domain where the velocity is set to one. A vanishing normal velocity is imposed on the boundaries.

Fig. 11 shows the isolines of the first component of the velocity field after 50 time steps. It can be seen that for the inviscid SWE, the velocity field is totally noisy. If the momentum diffusion term is not neglected anymore, the noise in the numerical solution can be removed for viscosity values around 5×10^5 m^2/s or more. These values, although quite important, are in agreement with viscosity values commonly used in OGCMs. One must remember that the initial conditions used in the present experiment are very different and much stronger than those commonly used in practice.

It must be pointed out that the stabilization method used for the P_1P_1 and the $P_1^{\perp}P_0$ element are not so close as they seem to be. The P_1P_1 element is stabilized thanks to the addition of a diffusion term to the continuity equation. This operation has no physical justification and is based on numerical considerations only. The stabilization of the $P_1^{\perp}P_0$ is based on the addition of a diffusion term to the momentum equation. This operation is physically realistic since there are momentum diffusion processes in oceanic flows and these processes are not neglected in more complex models. This gives a certain advantage to the $P_1^{\perp}P_0$ element over the stabilized P_1P_1 element.

The same results as in Sections 6.1 and 6.2 can be obtained by using an unstructured grid. However, as spurious oscillations are grid dependent, we have only shown results obtained on a structured grid since these are more "aesthetic".

6.3. Inertia-gravity wave propagation

This very simple test case considers the evolution of a Gaussian hill in a close system so as to see how a finite element scheme represents the propagation of inertia-gravity waves and if the use of

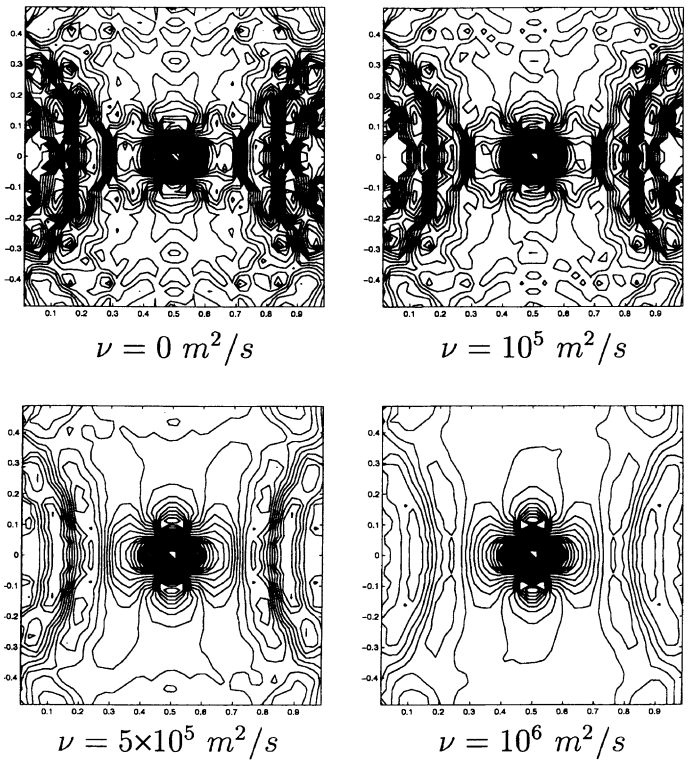

Fig. 11. Isolines of the first component of the velocity field for the $P_1^{\perp}P_0$ element with different viscosity values. The contour interval is 0.01 m/s.

an unstructured grid could generate noise in the numerical solution. The use of a closed domain also enables us to perform a mass and energy balance and thus to compare the stabilized P_1P_1 element ($\alpha = 5 \times 10^5$ m^2/s, $\nu = 0$) and the $P_1^{\perp}P_0$ element ($\alpha = 0$, $\nu = 0$) in term of mass and energy budget.

We consider a rectangular $L \times L$ domain ($L = 10^6$ m) in which the mean water depth is set to 2000 m. The Coriolis parameter and the gravitational acceleration are still set to 10^{-4} s^{-1} and 10 m s^{-2} respectively. Initially the fluid is at rest and the elevation (in meters) is described by the following expression:

$$\eta(x,y) = \exp\left(-\frac{((x - L/2)^2 + (y - L/2)^2)}{(L/4)^2} \right). \tag{34}$$

The unstructured mesh used in the simulation is composed of 2852 triangles and 7203 nodes (Fig. 12). The time step is set to 500 s.

The elevation field for the $P_1^{\perp}P_0$ element is given on Fig. 13. Qualitatively, the same results are obtained by using the stabilized P_1P_1 element. It can be seen that the use of an unstructured grid does not generate noise in the numerical solution. On the right hand side of the domain, the elevation field is sometimes a bit less sharp because of the coarser resolution in that region.

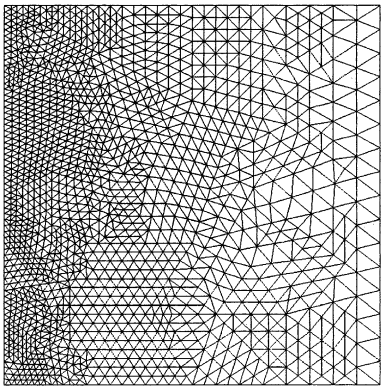

Fig. 12. Unstructured mesh used for inertia-gravity waves propagation. This mesh has 2852 elements.

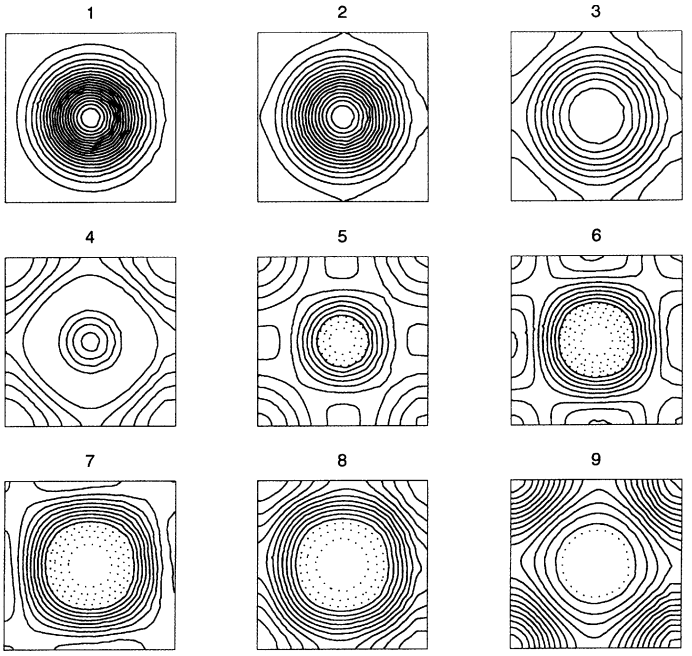

Fig. 13. Isolines of the surface elevation at different stages of gravity wave propagation and dispersion. These simulation have been done by using the triangular $P_1^{\perp}P_0$ element. The contour interval is 0.05 m. Dotted regions denote negative elevation.

To see if both schemes are mass preserving, we compute every 10 time steps the elevation field integral on the whole domain normalized by its initial value. Thus, the following quantity is computed:

$$M^n = \frac{|\int_\Omega \eta^n \, \mathrm{d}\Omega|}{|\int_\Omega \eta^0 \, \mathrm{d}\Omega|}, \tag{35}$$

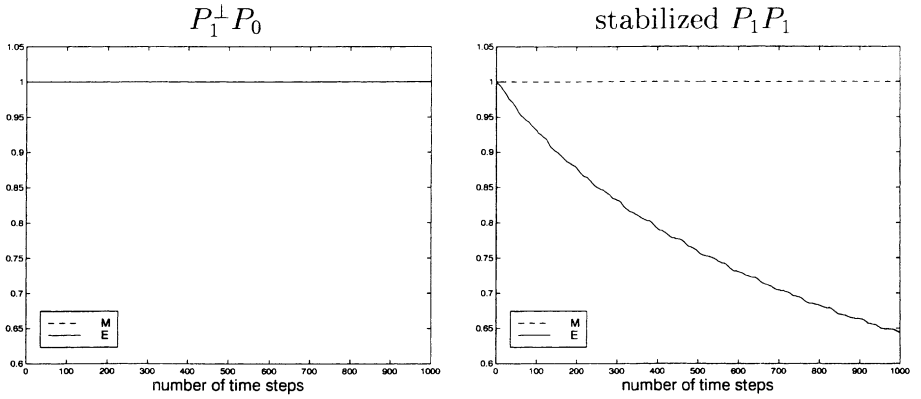

Fig. 14. Mass (- - -) and energy (—) budgets for both elements. For the $P_1^{\perp}P_0$ element ($\alpha = 0$, $\nu = 0$), both mass and energy are conserved (the two lines are one on the top of the other) whereas only the total mass of fluid is conserved by the stabilized P_1P_1 element ($\alpha = 5 \times 10^5$ m^2/s, $\nu = 0$). Mass variations around the initial value are of the order of 10^{-14} for both elements, energy variations around the initial value are of order of 10^{-10} for the $P_1^{\perp}P_0$ element.

where η^0 represents the initial elevation field. Results for both schemes are given on Fig. 14. For the $P_1^{\perp}P_0$ and the stabilized P_1P_1 element, (35) remains equal to one, the variations being around 10^{-14} which corresponds to computer roundoff errors. This means that both elements are mass preserving. This property is absolutely necessary to be able to use these elements for long term simulations.

It is possible to show the effect of the stabilization term used in the P_1P_1 scheme by computing the total energy of the flow normalized by its initial value. This quantity reads:

$$E^n = \frac{\int_\Omega \frac{1}{2}\rho(H(\mathbf{u}^n)^2 + g(\eta^n)^2)\,\mathrm{d}\Omega}{\int_\Omega \frac{1}{2}(H(\mathbf{u}^0)^2 + g(\eta^0)^2)\,\mathrm{d}\Omega}, \tag{36}$$

where $\mathbf{u}^0$ is the initial velocity field. Results for both schemes are given on Fig. 14. It can be seen that when the $P_1^{\perp}P_0$ element is used, the energy is conserved as the variations are of the order of 10^{-10}. However, the elevation diffusion term present in the stabilized P_1P_1 scheme leads to a decrease in the total energy of the flow. This shows that stabilization techniques have a non-negligible impact on the physics of the flow.

7. Conclusions

We have shown that the finite element equivalents of Arakawa's A-, B- and C-grids have the same characteristics as the corresponding finite difference discretizations. The finite element pairs corresponding to the A- and B-grids allow the existence of spurious elevation modes while the element corresponding to the C-grid allows the existence of spurious velocity modes. As a result, noise control procedures are required to be able to use these elements.

Among the three elements studied, the triangular $P_1^{\perp}P_0$ and the stabilized P_1P_1 elements are the only usable in an OGCM. This is mainly because both elements are mass preserving, do not allow

the existence of spurious elevation modes and propagate well inertia-gravity waves when the Rossby radius of deformation is resolved. When the deformation radius is not resolved, only the stabilized P_1P_1 element behaves properly. However, this element is stabilized by adding a diffusion term to the continuity equation. Such a stabilization method is not very attractive from a physical point of view since there are no mass diffusion processes. On the other hand, the spurious velocity oscillations generated by the $P_1^{\perp}P_0$ element while solving the inviscid SWE are filtered out in a more complex model where momentum diffusion is not neglected. This stabilization method, unlike the other, is physically realistic.

Acknowledgements

Emmanuel Hanert and Eric Deleersnijder are Research fellow and Research associate, respectively, with the Belgian National Fund for Scientific Research (FNRS).

References

Adcroft, A.J., Hill, C.N., Marshall, J.C., 1999. A new treatment of the Coriolis terms in C-grid models at both high and low resolutions. Monthly Weather Review 127 (8), 1928–1936.

Batteen, M.L., Han, Y.-J., 1981. On the computational noise of finite-difference schemes used in ocean models. Tellus 33, 387–396.

Bryan, K., 1969. A numerical method for the study of the circulation of the world ocean. Journal of Computational Physics 4, 347–376.

Deleersnijder, E., Campin, J.-M., 1995. On the computation of the barotropic mode of a free-surface world ocean model. Annales Geophysicae 13, 675–688.

DeMulder, T., 1997. Stabilized finite element methods for incompressible flows. Lecture notes, von Karman Institute.

Engelman, M.S., Sani, R.L., Gresho, P.M., 1982. The implementation of normal and/or tangential boundary conditions in finite-element codes for incompressible fluid flow. International Journal for Numerical Methods in Fluids 2, 225–238.

Haidvogel, D.B., Beckmann, A., 1999. Numerical ocean circulation modeling. In: Series on Environmental Science and Management. Imperial College Press.

Hanert, E., Deleersnijder, E., Legat, V., submitted for publication. Comments on 'Do not use a simple model when a complex one will do' by J.C.J. Nihoul, 1994, Journal of Marine Systems, 5, 401–406. Journal of Marine Systems.

Iron, B.M., 1970. A frontal solution program for finite element analysis. International Journal for Numerical Methods in Engineering 2, 5–32.

Killworth, P.D., Stainforth, D., Webb, D.J., Paterson, S.M., 1991. The development of a free surface Bryan–Cox–Semtner ocean model. Journal of Physical Oceanography 21, 1333–1348.

LeBlond, P.H., Mysak, L.A., 1978. Waves in the Ocean. In: Elsevier Oceanography Series. Elsevier.

Le Provost, C., Bernier, C., Blayo, E., 1994. A comparison of two numerical methods for integrating a quasi-geostrophic multilayer model of ocean circulations: finite element and finite difference methods. Journal of Computational Physics 110, 341–359.

Le Roux, D.Y., Staniforth, A.N., Lin, C.A., 1998. Finite elements for shallow-water equation ocean models. Monthly Weather Review 126 (7), 1931–1951.

Leygue, A., Legat, V., 2000. Domain decomposition and hybrid linear solvers for large 3d problems. In: Proc. 5th Nat. Congress on Theoretical and Applied Mechanics, Louvain-la-Neuve, Belgium, 23–24 May 2000. Belgian National Committee for Theoretical and Applied Mechanics, pp. 135–138.

Lilly, D.K., 1965. On the computational stability of numerical solutions of time-dependent non-linear geophysical fluid dynamics problems. Monthly Weather Review 93 (1), 11–26.

Lynch, D.R., Ip, J.T.C., Naimie, C.E., Werner, F.E., 1996. Comprehensive coastal circulation model with application to the Gulf of Maine. Continental Shelf Research 16, 875–906.

Mesinger, F., Arakawa, A., 1976. Numerical Methods used in Atmospheric Models. GARP Publications Series No. 17. WMO—ICSU.

Miglio, E., Quarteroni, A., Saleri, F., 1999. Finite element approximation of quasi-3d shallow water equations. Computer Methods in Applied Mechanics and Engineering 174, 355–369.

Murray, R.J., Reason, C.J.C., 2002. Fourier filtering and coefficient tapering at the North Pole in OGCMs. Ocean Modelling 4, 1–25.

Myers, P.G., Weaver, A.J., 1995. A diagnostic barotropic finite-element ocean circulation model. Journal of Atmospheric and Oceanic Technology 12, 511–526.

Raviart, P., Thomas, J., 1977. A mixed finite element method for 2nd order elliptic problems. In: Galligani, I., Magenes, E. (Eds.), Mathematical Aspects of the Finite Element Methods, Lecture Notes in Mathematics. Springer-Verlag, Berlin, pp. 292–315.

Walters, R.A., Carey, G.F., 1984. Numerical noise in ocean and estuarine models. Advances in Water Resources 7, 15–20.

Walters, R.A., Casulli, V., 1998. A robust finite element model for hydrostatic surface water flows. Communications in Numerical Methods in Engineering 14, 931–940.